Development and Testing of a Mechanical Model for the Cherenkov Telescope Array using a Single-CCD Pointing-Solution

Bachelorarbeit aus der Physik

vorgelegt von

Olaf Tönsing

Tag der Abgabe: 25. Juni 2019

Friedrich-Alexander-Universität Erlangen-Nürnberg

1. Gutachter: Prof. Dr. Christopher van Eldik
2. Gutachterin: Prof. Dr. Gisela Anton

Contents

1 Introduction

The question of our place in the universe has fascinated mankind at least since the beginning of recorded history. The study of the stars has been an important part of philosophy and science since the ancient Greeks. While in ancient times humans where limited to their own eyes, technological innovations such as the invention of the telescope in the early 17th century have made it possible to see ever smaller and fainter structures of the universe. The discoveries made by these improved instruments lead to a shift in our world view from believing we are the centre of the universe to realising that we are just orbiting one star in a galaxy of hundreds of billions of stars that is again just one galaxy in a universe with hundreds of billion galaxies. With the improved understanding of electromagnetism in the 19th century astronomers expanded the range on the electromagnetic spectrum in which observations could be made to radio waves and infrared radiation. Infrared telescopes allowed astronomers to see through dust clouds and observe the birthing processes of stars. The next big advancement in astronomy came with the advent of space based telescopes, since our atmosphere is opaque for electromagnetic radiation except for a few windows in the optical and infrared spectrum and for microwaves. But space based telescopes have the drawback of being size constrained by their launch vehicle. The James Webb Space Telescope, which will be the biggest space based telescope in history, will have a mirror diameter of just 6.5 m compared to earth based telescope that are currently in development with mirror diameters of 30 m, like the appropriately named Extremely Large Telescope. This size constraint becomes very important for observing very high energy (VHE) gamma-rays, since the flux over the energy of the photons drops by a power law. Above around 100 GeV the flux is too low to be observed by a technically feasible space based telescope. A solution that doesn't have this limitation is the so called Imaging Atmospheric Cherenkov Radiation (IACT) technique. It uses the atmosphere as a detection medium by observing the Cherenkov radiation produced by particles showers that are caused by a gamma-ray photon hitting the atmosphere. The Cherenkov Telescope Array (CTA) is an array of IACTs that is currently in development and is the successor of MAGIC, H.E.S.S. and VERITAS. It will consist of dozens of IACTs of three different sizes that are distributed over two sites, one in the northern and one in the southern hemisphere.
The so called *pointing* describes the ability to reconstruct the direction of an observed gamma-ray. This is done by using optical CCD cameras that are mounted on each telescope and track its orientation. The *mis-pointing*, the difference between the direction of the optical axis of the telescope and the CCD camera, is not constant but is mainly dependent on the orientation of the telescope, due to a variety of effects.

The goal of this thesis is to develop a mechanical model to describe these effects and to test this model using data from the MAGIC telescope.

2 Imaging Atmospheric Cherenkov Telescopes

2.1 Very-High-Energetic Gamma-Rays

Very-high-energetic (VHE) gamma-rays are photons with typical energies in the range of 100 GeV to 10 TeV. While most of the light that we can see in the sky with our eyes is produced by thermal radiation, the temperature needed to produce VHE gamma-rays exceeds that of any known object in the universe by several orders of magnitude (A black body that has its energy of maximum flux at 100 GeV has to have a temperature of over 2×10^{14} K). Therefor other processes are needed to produce these photons. One such process is the inverse Compton-scattering, in which a high energy electron collides with a low energy photon and transmits it's energy to that photon.

$$e_{\texttt{VHE}} + \gamma_{\texttt{low energy}} \rightarrow e_{\texttt{low energy}} + \gamma_{\texttt{VHE}} \tag{1}$$

The VHE electrons are produced in cosmic particle accelerators, for example in supernova remnants, pulsar wind nebulae or active galactic nuclei (AGN). A map of all currently known VHE gamma-ray sources and their types can be found in Figure 1. Supernovae remnants are produced after stars with high enough masses

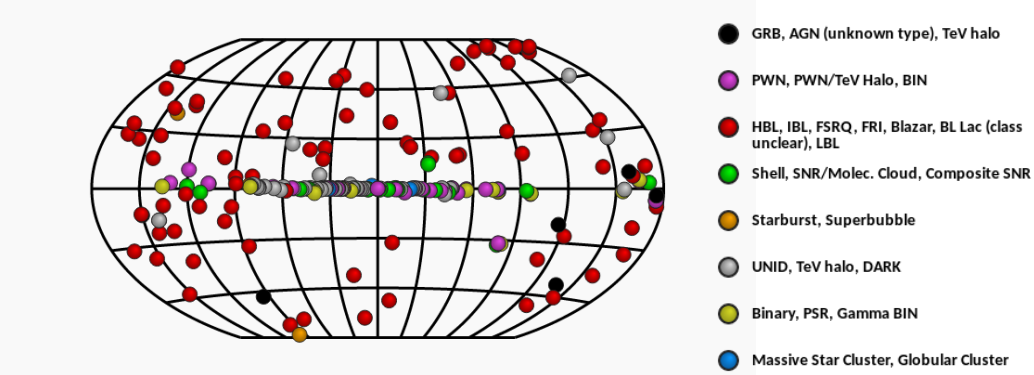

Figure 1: TeV gamma-ray sources in galactic coordinates (Scott Wakely, 2016).

reach their end of life and explode. This explosion creates a shock front with strong magnetic fields, in which electrons are scattered and accelerated. A pulsar is a neutron star with a very strong magnetic field that is tilted in respect to its rotational axis which emits electromagnetic radiation. When the magnetic field axis of such a neutron star, which rotates with a frequency of about one rotation per second, points at the earth, a short radio pulse can be detected and the neutron star is called a pulsar. Through interactions of the magnetic field of a pulsar with the surrounding matter charged particles can be accelerated to very high energies.

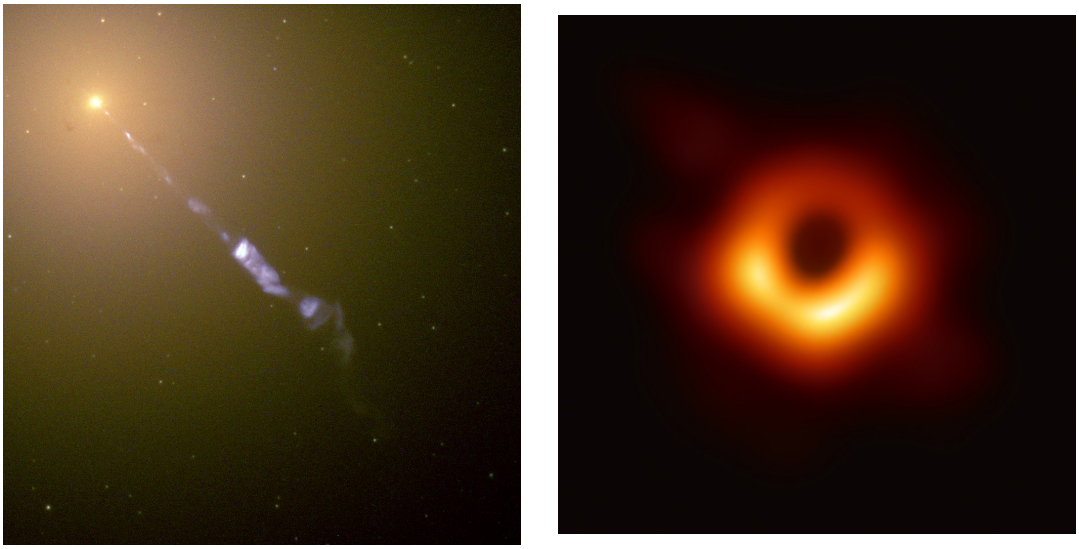

Figure 2: Left: The galaxy M87 with it's jet (Wikipedia contributors, 2019). Right: An image of the black hole at the centre of M87 (EHT Collaboration et al., 2019).

Active galactic nuclei are cores of galaxies which emit a lot of energy. They are believed to be powered by converting the gravitational energy of matter falling into a super-massive black hole into light. The falling matter produces a accretion disk that surrounds the black hole. Some AGN also produce jets perpendicular to the accretion disc. In those jets particles can be accelerated in shock fronts. An example for an AGN with a jet and the black hole powering the AGN can be seen in Figure 2

2.2 Air-Showers and Cherenkov Radiation

If a VHE gamma-ray photon hits the earths atmosphere it produces an electron-positron pair in the field of an atomic nuclei. These particles then produce additional gamma-rays through Bremsstrahlung, which in turn produces more electron-positron pairs and so on. This leads to a cascading effect and the production of a so called air-shower.

As long as the velocity of a charged particle, which is travelling through a medium, is larger than the speed of light in that medium, Cherenkov radiation is emitted by this particle. This radiation is being emitted in a cone around the particle track (see Figure 3), with the opening angle of this cone being

$$\cos\theta = \frac{1}{n\beta}, \tag{2}$$

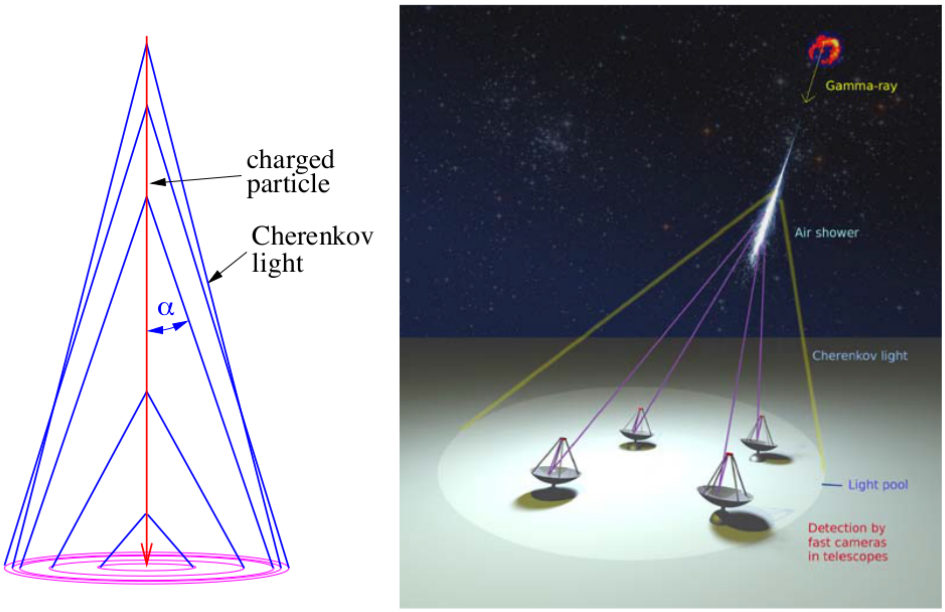

Figure 3: Left: Cherenkov cone produced by a single gamma-ray hitting the atmosphere at a right angle (Bernlöhr, 2009).
Right: Detection principle of a gamma-ray by IACTs (Bernlöhr, 2009)

with $\beta = \frac{v}{c}$ where v is the velocity of the particle and with n being the refractive index of the medium. The Cherenkov radiation hits the ground and illuminates a circle with a typical radius of about 125 m. The Cherenkov flash lasts for a few nanoseconds (Bernlöhr, 2009). To detect this Cherenkov radiation so called *Imaging Atmospheric Cherenkov Telescopes* (IACTs) are used. Since the intensity of these Cherenkov flashes is very low, IACTs typically have large mirrors. IACTs need fast cameras to record the very short Cherenkov flashes, which is why photomultiplier tubes or silicon photomultipliers are used. These fast cameras have the additional advantage of being able to distinguish the Cherenkov flashes from the background. Two IACTs that are currently in operation or are being constructed are introduced in the next chapters.

2.3 Major Atmospheric Gamma-Ray Imaging Cherenkov Telescopes

The Major Atmospheric Gamma-Ray Imaging Cherenkov Telescope (MAGIC) is an IACT that is located in La Palma. It was completed in the year 2003 and commissioned in 2004. It has a mirror with a diameter of 17 m and an area of 234 m^2, as can be seen in Figure 4. It was designed as a light weight telescope

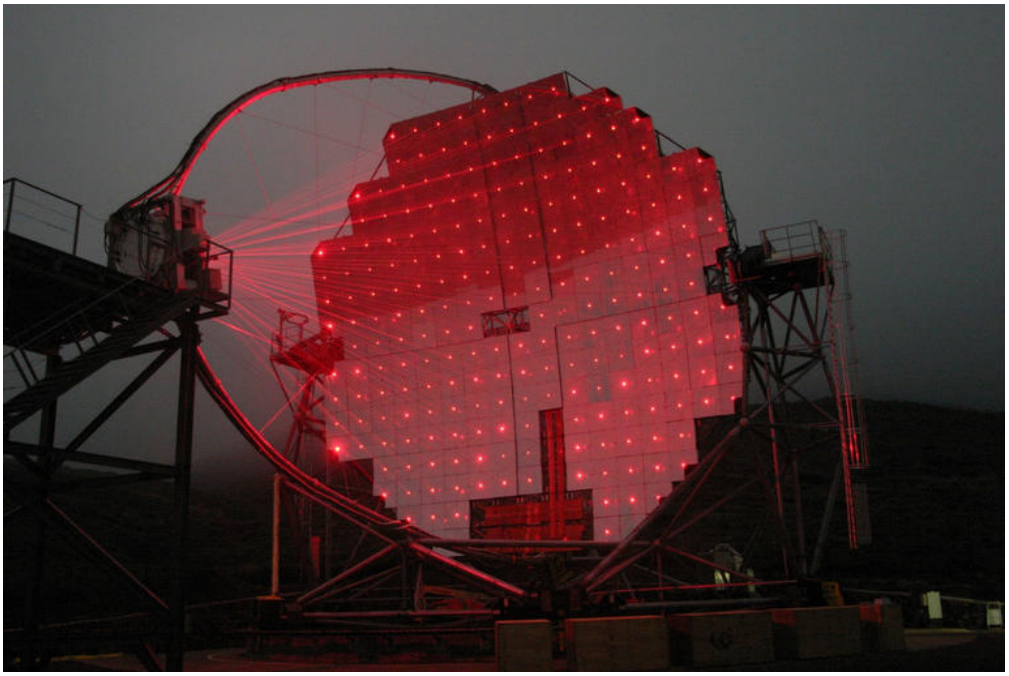

Figure 4: The MAGIC telescope during mirror alignment in a foggy night (Robert Wagner, 2004)

to allow for fast slewing. This is needed to observe short lived gamma-ray bursts (GRB). It is mounted on an altazimuth mount and has a field of view of 3.5° to 3.8°. It has an angular resolution for gamma-ray events of around 0.1° at energies of $> 200\,\mathrm{GeV}$, but for a point source this resolution improves by the square root of observed events and is ultimately limited by the tracking accuracy of the telescope, which is $\simeq 0.01°$ (Bigongiari, 2005).

2.4 Cherenkov Telescope Array

The Cherenkov Telescope Array (CTA) is the planned successor to the present IACTs MAGIC, H.E.S.S and VERITAS. It is currently being designed and tested by an international collaboration. For the CTA to be able to observe the whole sky the array is split into a northern site situated in La Palma and a southern site in Paranal in Chile (the proposed layout can be found in Figure 5). The southern sites main objective is to record gamma-ray emissions from inside our own galaxy while the northern site will search for extra galactic sources. The array will consist of three different types of telescopes. There are different proposals for each of the telescopes and it has not yet been decided which proposal will be used, but they share common design goals. The Small Sized Telescope (SST) will have a

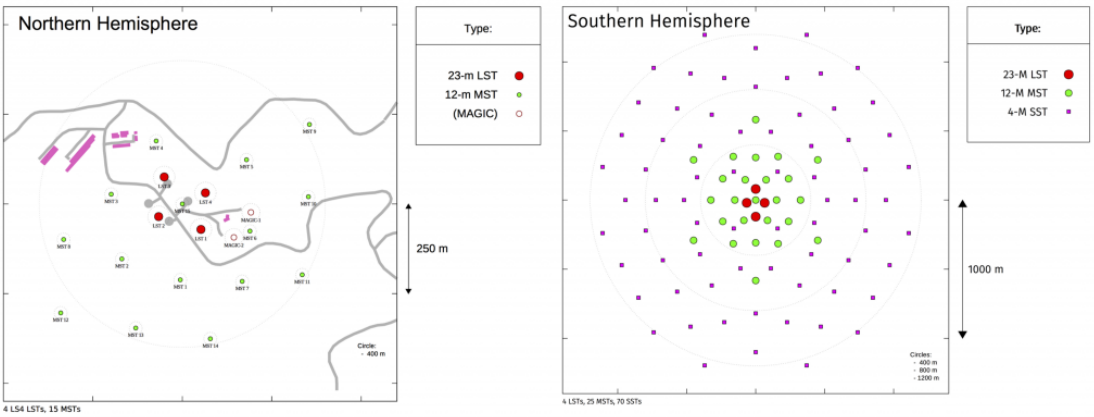

Figure 5: The proposed layout of the Cherenkov Telescope Array. (CTA collaboration, 2019)

mirror diameter of 4 m and will be responsible to observe gamma-ray events with energies of over 10 TeV. These events occur at low rates, which requires a large covered area, but they are very bright so no large mirror area is needed to observe them. The SSTs will only be used on the southern site to observe gamma-ray events inside our own galaxy. The workhorse of the CTA will be the Medium Sized Telescope (MST). It will be responsible for the core energy range of between 100 GeV to 10 TeV and will have a mirror size of 12 m. The design goal for the MST is a pointing precision of less than 7″. The CTA is currently planned to have 40 MSTs, 25 at the southern and 15 at the northern site. A small number of Large Sized Telescope will be responsible for energies below 100 GeV. Gamma-ray events with these energies are fairly common, but the luminosity of these events is very low which is why the LSTs will have a mirror diameter of 23 m (CTA collaboration, 2019). The angular resolution goal of the CTA can be found in Figure 6. For point sources this resolution will again improve with the square root of the number of events and will be limited by the pointing precision of the telescopes.

2.5 Astrometry and Pointing

Pointing refers to the ability to extract the position of stars on the three dimensional celestial sphere from the two dimensional image plane and to the ability to determine the direction of the telescope. In optical astronomy astrometry describes the ability to precisely measure the position and movement of stars. By obtaining a catalogue of stars with precisely known positions, such as the Gaia catalogue which contains the positions of more than a million stars, one can use those stars as reference points for measuring the position or movement of unknown

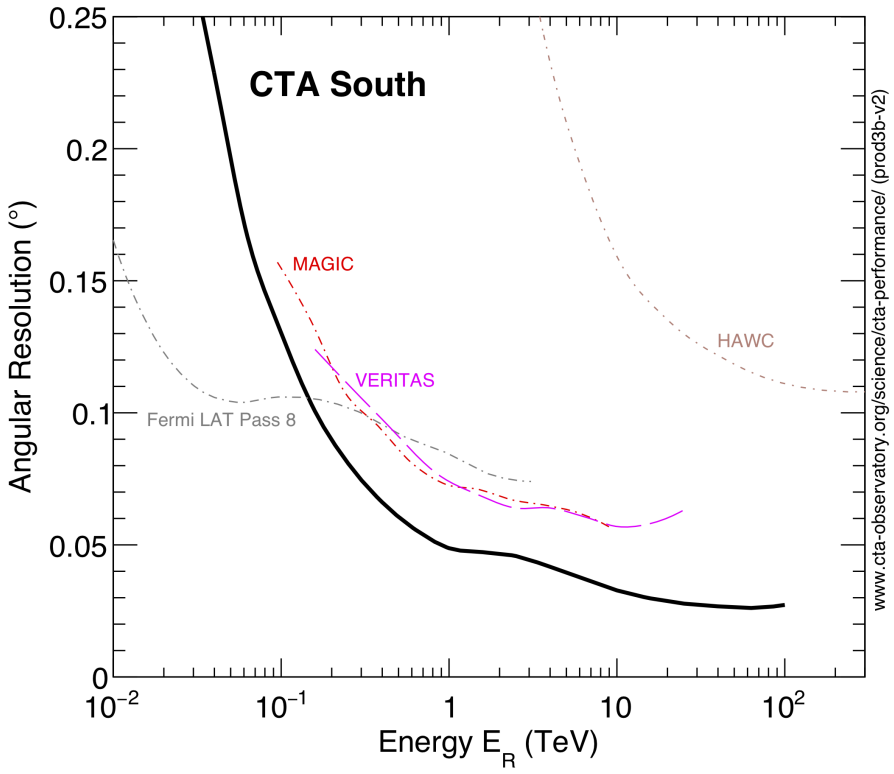

Figure 6: The angular resolution of CTA compared to previous IACTs (CTA collaboration, 2019).

objects. For IACTs this is not possible since there are only on the order of 100 known reference sources (see Figure 1). This makes it very likely that there is no reference source in a typical field of view for an IACT of a few degrees. Therefor a different approach is needed for IACTs. The concept used by MAGIC is a two CCD concept. The SkyCCD is responsible for determining the direction the telescope is pointing in by taking images of the nights sky, extracting star positions from that image and fitting them to known positions from star catalogues. The LidCCD observes the stars mapped on the lid of the Cherenkov camera and LEDs attached to that lid and calculates the deformations of the telescope. This allows the use of a fitting routine to get the true pointing of the Cherenkov camera. The SingleCCD concept combines the SkyCCD and LidCCD into a single so called PointingCCD camera with a larger field of view. An illustration of this concept can be found in Figure 7.

The advantages of this concept are lower costs and less points of failure, leading to less downtime of the telescope for maintenance purposes. One drawback

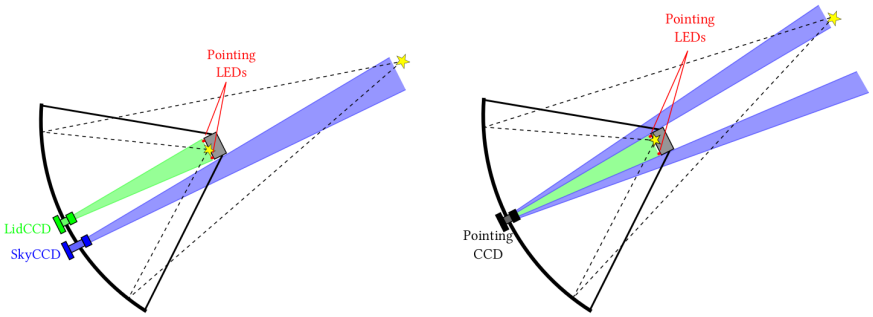

Figure 7: Left: Concept of LidCCD and SkyCCD mounted on a telescope. Right: Concept of a single PointingCCD that combines the LidCCD and SkyCCD. (Herbich, 2010)

is that the Cherenkov camera obstructs a large part of the field of view of the PointingCCD, which makes the fitting of the position of known stars more prone to failure than for the SkyCCD. A PointingCCD camera has been installed on the MAGIC telescope to test this concept.

3 MST Pointing Corrections

3.1 Motivation

In this chapter a mechanical model will be developed to describe the direction dependent mis-pointing. A mechanical model is normally calibrated by using dedicated pointing runs, in which known positions in the sky are targeted and the parameters describing the model are calculated. Since the PointingCCD used for this thesis is installed on the MAGIC telescope which is actively doing research this is not possible. Therefor images from the PointingCCD recorded during normal operations of the telescope are used. It is important to note that the model developed in this thesis does not take data from the LEDs or stars projected on the camera lid of the telescope into account. It can therefor just describe effects that influence the whole telescope and not describe any effects that are caused by for example the bending of the camera mast under its own weight or the bending of the mirrors. To fully describe the telescope these additional effects have to be taken into account in a future improvement of this model.
As has been explained in the last chapter it is possible to directly reconstruct the current pointing direction of the telescope from optical images taken by the PointingCCD. This can be done with much better accuracy then with a mechanical model, the accuracy of a reconstruction algorithm can be as good as a few arcseconds (Tiziani, 2015), while the accuracy of a mechanical model is typically in the range of tens of arcseconds (Romaszkiewicz, 2006). This leaves the question why a mechanical model is needed to describe the pointing of a telescope. The main reason is that a mechanical model enables offline pointing corrections to the data while the PointingCCD needs to always take images at the same time at which observations are being made. This becomes important if the PointingCCD breaks for some reason and needs to be repaired. The mechanical model allows the telescope to continue operating with reduced, but still decent pointing accuracy until the PointingCCD is repaired.
In the following chapters the mechanical model will be developed starting with the necessary coordinate systems and transformations.

3.2 Coordinate Systems and Transformations

In astronomy different coordinate systems are used depending on the type of observation made. The most common ones for earth based telescopes are the equatorial and horizontal coordinate systems.

Equatorial Coordinate System

The equatorial coordinate system, also known as the RA-Dec system, is a widely

used system to map the position of stars on the celestial sphere. The position of an object in the equatorial coordinate system is described by the declination δ and the right ascension α. It is not coupled to the daily rotation of the earth, which means that in a first approximation the position of a star is independent of the time of the observation.

Horizontal Coordinate System

In the horizontal coordinate system, also known as the Alt-Az system, the position of a star in the sky is described by two spherical coordinates, the altitude and the azimuth. The altitude describes the elevation of a point above the horizon and ranges between $-90°$ and $90°$, with $90°$ describing the zenith. The azimuth describes the position of a point on the horizontal plane and ranges between $0°$ and $360°$, with $0°$ describing north and $90°$ east. The position of a star in the horizontal coordinate system is therefore dependent on the position of the observer and the time of the observation. The advantages of the horizontal system are, that corrections applied by the mechanical model, which will be described in subsection 3.5, are directly dependent on the altitude and azimuth. In the pointing algorithm all rotations will be applied in a Cartesian coordinate system. Since the Alt-Az coordinate system is a left handed system, this has to be taken into account in the transformations. The transformation between the horizontal coordinate system and the Cartesian coordinate system is given by the following equations:

$$\begin{aligned} x &= \cos(alt) \cdot \cos(az) \\ y &= \cos(alt) \cdot \sin(az) \\ z &= \sin(alt) \end{aligned} \tag{3}$$

The Cartesian coordinate system is a right handed system, this means that the y-axis is pointing west and the x-axis north. After the rotations the vectors have to be transformed back into the horizontal coordinate system, which is done by the following equations:

$$\begin{aligned} alt &= \frac{180}{\pi} \arcsin(z) \\ az &= -1 \cdot (\frac{180}{\pi} \text{arctan2}(x, y) - 540) \mod 360 \end{aligned} \tag{4}$$

with the function arctan2, that is defined by

$$(x, y) \mapsto \begin{cases} \arctan\left(\frac{y}{x}\right) & \text{for } x > 0 \\ \arctan\left(\frac{y}{x}\right) + \pi & \text{for } x < 0, y > 0 \\ \pm\pi & \text{for } x < 0, y = 0 \\ \arctan\left(\frac{y}{x}\right) - \pi & \text{for } x < 0, y < 0 \\ +\frac{\pi}{2} & \text{for } x = 0, y > 0 \\ -\frac{\pi}{2} & \text{for } x = 0, y < 0 \end{cases} \tag{5}$$

The value range of the function arctan2 is $[-\pi, \pi]$. Because the azimuth angle is counterclockwise in this definition, the result of the arctan2 function is multiplied by -1. To get the range to $[0°, 360°]$, $540°$ is added and the modulo operation is applied. This is done to make sure that no values larger than $360°$ or smaller than $0°$ are possible, which might arise due to numerical imprecision.

3.3 Rotation Matrices

To apply the correction factors determined by the mechanical model the algorithm has to be able to rotate vectors in three dimensions. For simplicity purposes all rotations are done in Cartesian coordinates. The rotation around the three axes of the Cartesian coordinate system are described by the following matrices. Rotation around the x-axis:

$$R_{x,\theta} = \begin{bmatrix} 1 & 0 & 0 \\ 0 & \cos\theta & -\sin\theta \\ 0 & \sin\theta & \cos\theta \end{bmatrix} \tag{6}$$

Rotation around the y-axis:

$$R_{y,\theta} = \begin{bmatrix} \cos\theta & 0 & \sin\theta \\ 0 & 1 & 0 \\ -\sin\theta & 0 & \cos\theta \end{bmatrix} \tag{7}$$

Rotation around the z-axis:

$$R_{z,\theta} = \begin{bmatrix} \cos\theta & -\sin\theta & 0 \\ \sin\theta & \cos\theta & 0 \\ 0 & 0 & 1 \end{bmatrix} \tag{8}$$

The z-axis in Cartesian coordinates is in a first approximation equal to the azimuth axis in the Alt-Az coordinate system, errors from this assumption are discussed in subsubsection 3.5.2. Therefor it is used to describe rotations in azimuth. In addition to these standard rotation matrices a way to describe a rotation around an arbitrary axis is needed to describe a rotation around the altitude-axis, since this axis is dependent on the direction in azimuth in which the telescope is pointing. This is achieved by using Rodrigues' rotation formula in its vector form

$$\mathbf{v}_{\text{rot}} = \mathbf{v}\cos\theta + (\mathbf{k} \times \mathbf{v})\sin\theta + \mathbf{k}(\mathbf{k} \cdot \mathbf{v})(1 - \cos\theta). \tag{9}$$

Here the vector $\mathbf{k}$ is the unit vector describing the axis around which $\mathbf{v}$ should be rotated. In the case of a rotation around the altitude-axis, $\mathbf{k}$ can be parameterized by the following vector:

$$\mathbf{k}_{az} = \begin{pmatrix} \cos(az + 90°) \\ \sin(az + 90°) \\ 0 \end{pmatrix} \tag{10}$$

3.4 Fitting Algorithm

The fitting algorithm takes the directional data of the PointingCCD camera and that of the telescope in horizontal coordinates. It tries to minimise the difference between the two by applying a mechanical model as described in subsection 3.5. The residual to be minimised is calculated by applying the model to all data points of the PointingCCD and then summing the squared angular differences between the corrected PointingCCD vectors and the telescope vectors. The minimizer is based on the Nlopt library by (Johnson, 2019) and uses the Controlled Random Search 2 (CRS2) algorithm developed by (Kaelo and Ali, 2006). This choice was made because the CRS2 algorithm searches for global minima. The CRS2 algorithm is a bound constrained algorithm, the choices for the bounds are discussed in detail in subsection 4.1. For the termination condition a relative tolerance of 1×10^{-9} is chosen, because this leads to high precision while keeping the run-time of the algorithm shorter than one minute.

3.5 Mechanical Model

The main factors that cause mis-pointing are explained in the following chapters. The mechanical reasons that lead to this mis-pointing are adapted from (Lennarz, 2012), the corrections for the mis-pointing were developed separately.

3.5.1 Constant Offset

The dominant effect is a constant offset between the optical axis of the telescope and that of the PointingCCD. This is probably caused by mounting errors, since it is difficult to perfectly align the PointingCCD with the optical axis of the MAGIC telescope. This leads to a constant angular offset, which in Cartesian coordinates is independent of the direction in which the MAGIC telescope is pointing. The parameters describing this effect are Δalt and Δaz. Δalt and Δaz are the offset in Alt-Az between the optical axis of the PointingCCD and of the MAGIC telescope while the MAGIC telescope is pointing at $(alt, az) = (0°, 0°)$. Since the Alt-Az coordinate system is a Curvilinear coordinate system, the offset in altitude and azimuth is not constant. To get the offset for an arbitrary direction (alt, az), a function called *proportinal-rotation-of-two-vectors* was created. The two vectors are the origin ($\mathbf{v}_1 = (0, 0)$) and the offset ($\mathbf{v}_2 = (\Delta alt, \Delta az)$). Both vectors are transformed into cartesian coordinates. Then a rotation around the azimuth axis, which in Cartesian coordinates is the z-axis, by az degrees is applied:

$$\mathbf{v}'_{1,\mathtt{car}} = \mathrm{R}_z\,(az) \cdot \mathbf{v}_{1,\mathtt{car}}$$
$$\mathbf{v}'_{2,\mathtt{car}} = \mathrm{R}_z\,(az) \cdot \mathbf{v}_{2,\mathtt{car}}$$

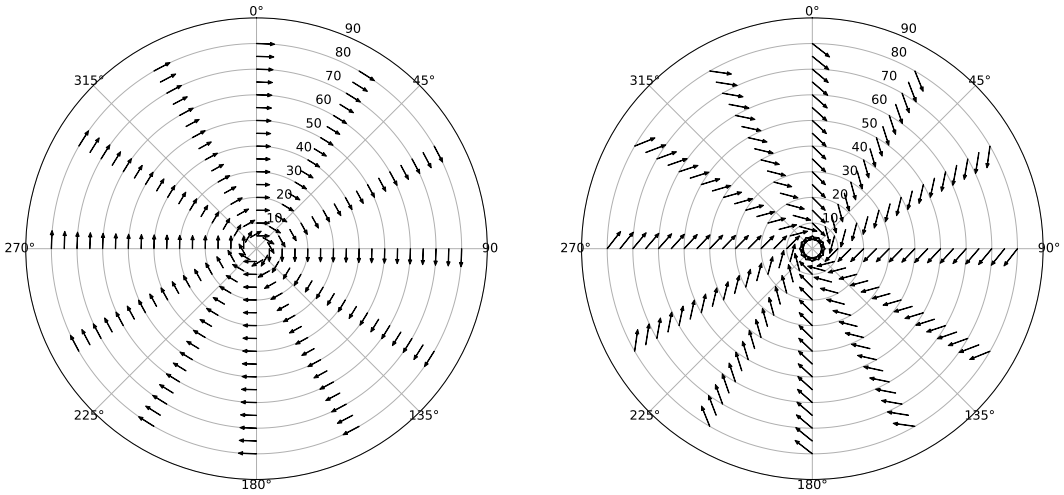

(a) (b)

Figure 8: Polar plot of the effect of a constant offset between the optical axis of the PointingCCD and that of the telescope. The radial axis is the zenith, e.g. $90° - alt$, the polar axis is the azimuth. In the left image an offset in (alt, az) of $(0°, 5°)$ was chosen, in the right image an offset of $(5°, 5°)$. One can see that the arrow length, and therefor the angular offset, are independent on the pointing direction.

After that a rotation around the altitude axis of $\mathbf{v}'_{1,\texttt{car}}$ is performed for both vectors. This means applying Rodrigues' rotation formula as described in subsection 3.3 around the axis $\mathbf{k}_{az}$ to both vectors. The result of such a rotation can be seen in Figure 8.

3.5.2 Non-Verticality of the Azimuth Axis

The azimuth axis doesn't have to be perfectly aligned with the z-axis. This can be caused by construction errors and shifting ground levels over time. This effect can be parameterized with two parameters λ and β. λ describes the direction of maximum deflection and β describes the amplitude of the deflection. To calculate the deflection of a vector $\mathbf{v}$ at a given point (alt, az), it is first transformed into

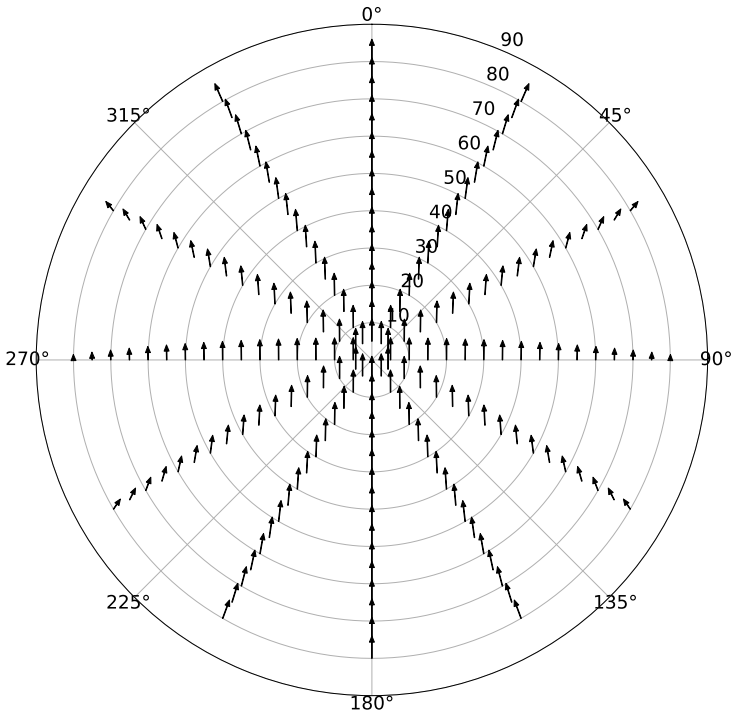

Figure 9: Demonstration of the effect of a non-vertical azimuth axis. The values for (λ, β) are $(180°, 6°)$.

Cartesian coordinates and the axis, that is perpendicular to λ, is calculated

$$\mathbf{k}_\lambda = \begin{pmatrix} \cos(\lambda + 90°) \\ \sin(\lambda + 90°) \\ 0 \end{pmatrix}. \tag{11}$$

Then the vector is rotated around the axis $\mathbf{k}_\lambda$

$$\mathbf{v}_{\text{rot}} = \mathbf{v}\cos\beta + (\mathbf{k}_\lambda \times \mathbf{v})\sin\beta + \mathbf{k}_\lambda(\mathbf{k}_\lambda \cdot \mathbf{v})(1 - \cos\beta). \tag{12}$$

The difference to a normal rotation around an altitude-axis is, that here all vector, independent of their position on the sphere, are rotated around the same axis. This is visualised in Figure 9.

3.5.3 Non-Perpendicularity of the Axes

Due to fabrication and construction errors the altitude and azimuth are in general not perfectly perpendicular. This causes an additional offset that is dependent

on the altitude, but is independent on azimuth because the correction applied in subsubsection 3.5.2 corrects the azimuth axis to be vertical. This shift can be parameterized with a single parameter δ, where the angle between the axes is $90° - \delta$. To get the correction for a given vector $\mathbf{v} = (alt, az)$, first the unit vector of the projection of that vector on the xy-plane

$$\hat{\mathbf{v}}_{\mathtt{proj}} = \begin{pmatrix} \cos az \\ \sin az \\ 0 \end{pmatrix} \tag{13}$$

and the non-shifted altitude axis

$$\hat{\mathbf{e}}_{alt} = \begin{pmatrix} \cos\left(az + 90°\right) \\ \sin\left(az + 90°\right) \\ 0 \end{pmatrix} \tag{14}$$

is calculated. Then the altitude axis is rotated by δ degrees around $\hat{\mathbf{v}}_{\mathtt{proj}}$ using Rodrigues' rotation formula

$$\hat{\mathbf{e}}_{alt}^{'} = \hat{\mathbf{e}}_{alt} \cos\delta + (\hat{\mathbf{v}}_{\mathtt{proj}} \times \hat{\mathbf{e}}_{alt}) \sin\delta + \hat{\mathbf{v}}_{\mathtt{proj}} (\hat{\mathbf{v}}_{\mathtt{proj}} \cdot \hat{\mathbf{e}}_{alt})(1 - \cos\delta), \tag{15}$$

so that the angle between the axes is now $90° - \delta$. Finally $\hat{\mathbf{v}}_{\mathtt{proj}}$ is rotated around the shifted altitude axis by alt degrees again using the Rodrigues' rotation formula:

$$\mathbf{v}^{'} = \hat{\mathbf{v}}_{\mathtt{proj}} \cos alt + (\hat{\mathbf{e}}_{alt}^{'} \times \hat{\mathbf{v}}_{\mathtt{proj}}) \sin alt + \hat{\mathbf{e}}_{alt}^{'} (\hat{\mathbf{e}}_{alt}^{'} \cdot \hat{\mathbf{v}}_{\mathtt{proj}})(1 - \cos alt) \tag{16}$$

$\mathbf{v}^{'}$ is now the vector corrected for the non-perpendicular axes. The effect of this can be seen in Figure 10. This correction has mainly an effect on the azimuth, and the amplitude of the azimuth correction is strongly dependent on the altitude.

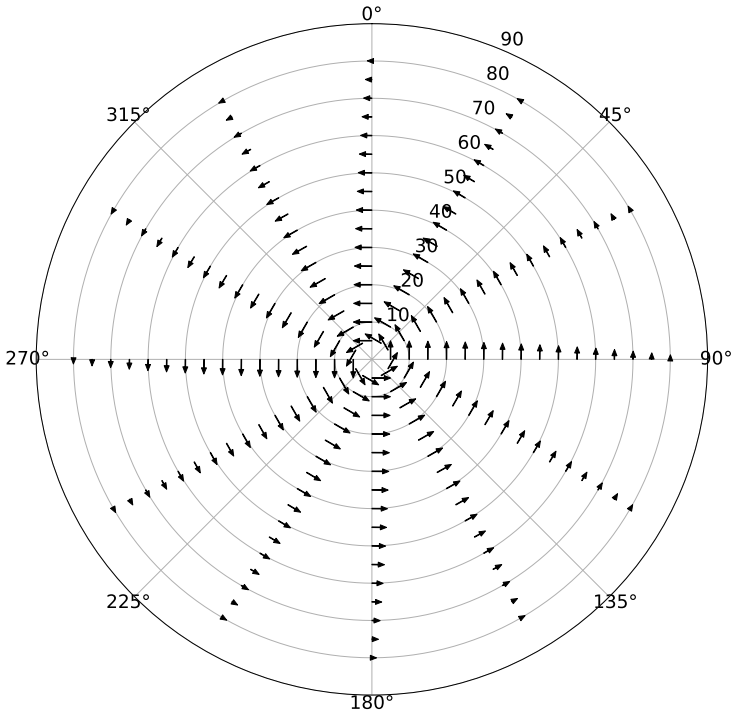

Figure 10: Demonstration of the effect of non-perpendicular axes. The value for δ is 5°.

4 Application of the Pointing Model

In this chapter the mechanical model developed in the previous chapter will be tested on both real and simulated data to find out how well the developed model describes real data and how sensitive the fitting parameters are to noise. Also an analysis on and discussion of the remaining residuals will be performed.

4.1 Testing on Simulated Data

For a first test of the fitting algorithm simulated data was used. This was done to test the stability of the algorithm. Data was simulated on an evenly spaced grid with distances in (alt, az) of $(5°, 15°)$. The parameters used for this simulation can be seen in Table 1. Then Gaussian noise with a mean of 0° and a standard deviation of 0.3° was added to each data point. This was done for two reasons.

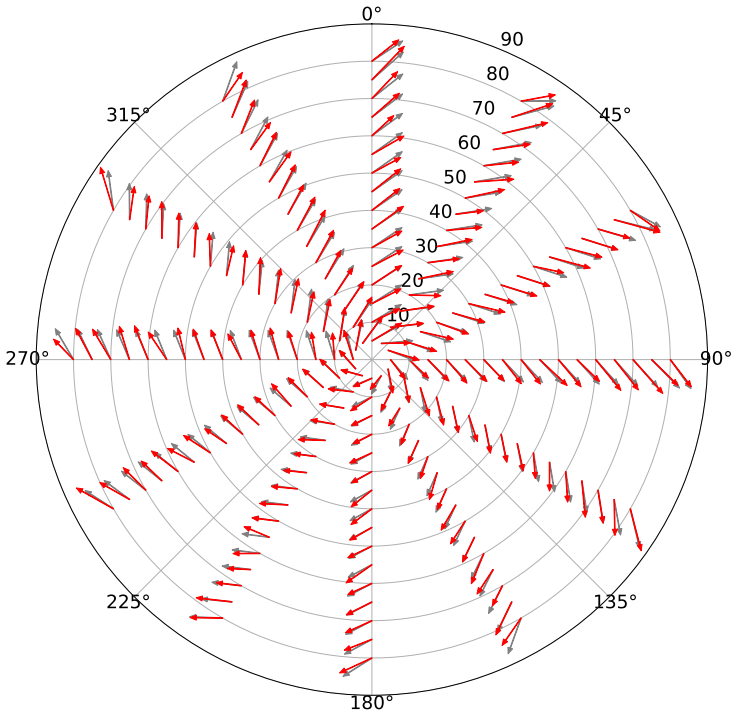

Figure 11: The red arrows are the simulated data with Gaussian noise, the grey arrows the fitted model. All arrows are scaled by a factor of 2.5 for better visibility.

parameter	simulation-parameter	fitted-value	percentage difference
Δalt	$-1.8°$	$-1.766°$	$1.89\,\%$
Δaz	$2.1°$	$2.062°$	$1.81\,\%$
λ	$130°$	$129.747°$	$1.81\,\%$
β	$0.7°$	$0.680°$	$2.86\,\%$
δ	$-0.6°$	$-0.630°$	$5\,\%$

Table 1: Fitting parameters for the fit on simulated data.

Firstly to see how small deviations will impact the fitting parameters and secondly because the fitting algorithm doesn't terminate if there is an exact solution with a residual of 0 if it is used in the relative tolerance mode, which is the mode also used in fitting real data. The starting parameters for the fit where 0 for each parameter to test if the algorithm can find a solution with no prior information. The upper and lower bounds are relevant for the parameters λ and β. For λ they have to be $(0°, 360°)$. If the range is smaller than that, the global minimum might not be in the range, if it is bigger there might be two or more solutions for λ that are equally good, and the algorithm won't terminate. For β there is a similar issue. If negative values are allowed and the range for λ is $(0°, 360°)$, then there are again two equally good solutions for λ and the algorithm won't terminate. The range for the other parameters have almost no effect on whether or not the algorithm terminates, as long as they are not too large, since this will lead to the same effect as for λ, just on the time it takes to find a solution. This is why they were all set to $\pm 5°$. The simulated data and fitted model can be seen in Figure 11, the fitted parameters and the percentage difference, meaning $\frac{|\text{simulationparameter} - \text{fittedvalue}|}{\text{simulationparamter}}$, in Table 1. All parameters have errors from the model of $\leq 5\,\%$, which is completely explained by the random noise added to the simulated data. This firstly shows that the fitting algorithm is capable of finding known solutions and that the parameters are stable for small deviations.

4.2 Application of the Model on Real Data

To really test the mechanical model it has to be applied to real data. The data was obtained by using the reconstruction algorithm developed by (Tiziani, 2015) to get the pointing data of the PointingCCD, and by using the log files of the MAGIC telescope to get the pointing data of the telescope. The reconstruction algorithm fits the position of known stars to the images captured by the PointingCCD and returns the pointing direction of the camera centre in both horizontal and equatorial coordinates. Since all effects are dependent on the altitude and azimuth the horizontal coordinates were used. The exposure time of the images captured by

the PointingCCD was 10 s. If there are not enough stars in an image that were matched to catalogued stars then the reconstructed coordinates aren't accurate, which is why all images where less than 10 stars were matched are discarded. To be able to compare the directions of the optical axis of the PointingCCD with that of the MAGIC telescope they have to be matched. This is done using the Unix timestamps of the observation time. Since the MAGIC telescope is mounted on a horizontal mount it has to actively correct it's orientation to keep pointing at the same object in the sky. This leads to the stars captured by the PointingCCD to not be point-like but smeared out over multiple pixels. Since the reconstruction

parameter	fitted-value
Δalt	$-1.903°$
Δaz	$1.538°$
λ	$235.456°$
β	$0.017°$
δ	$-0.663°$

Table 2: Parameter of the fit of the model to data from the MAGIC telescope and the PointingCCD

algorithm fits the centre of mass of the stars, this can be corrected by taking the position from the log files at the observation time of the PointingCCD plus 5 s. This data is then fed to the fitting algorithm. The fitting parameters can be found in Table 2. Since the fitting is done with a minimising algorithm and not the standard linear least square fit, there are no errors on the fitting parameters. The residual after the fit, meaning the summed squared angular difference between the model and the data, is $0.0116\,°^2$.
The fitted model and every sixteenth data point are plotted in Figure 12. Not all data points were plotted since there are about 4000, which would make the plot unreadable. The data points are not isotropic since the data acquisition was done during the normal operation time of the telescope and no dedicated pointing runs were performed. This also means that the fitting algorithm strongly prioritises minimising the residuals in areas with a high density of data points. The effects that this prioritisation can have will be discussed in subsection 4.4.

4.3 Discussion of Residuals

To see how well the fitting algorithm describes the data, the residuals between the model and the data are calculated and analysed. The residuals are plotted in Figure 13. The residuals are smaller in areas with a lot of data points, because the current algorithm treats all points equally and just tries to minimise the sum

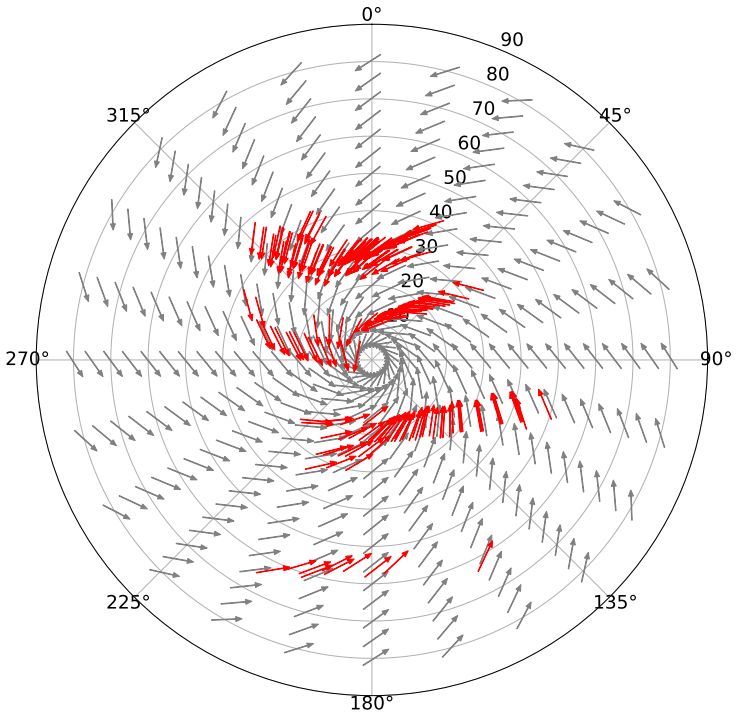

Figure 12: Black arrows is the difference between the optical axis of the MAGIC telescope and the reconstructed direction of the PointingCCD, grey arrows are the model fitted to the data. All arrows are scaled by a factor of 3.

of the residuals. This leads to fitting parameters that favour areas with a high density of points such as at an azimuth between 0° and 30° and a zenith angle between 30° and 40°. To see if there are any remaining effects that are dependent on altitude and azimuth that are not yet taken into account by the model, the residuals in altitude/azimuth are plotted over altitude/azimuth.

4.3.1 Altitude Residuals

The altitude residuals over the altitude are plotted in Figure 14. One can clearly see a correlation of the residuals in altitude with the altitude. These residuals likely originate from a mechanical effect, because there is little spread around a well defined correlation which excludes outside factors like wind or temperature, because the data was taken over several months.

Therefore geometric functions are considered first to describe the effect. There

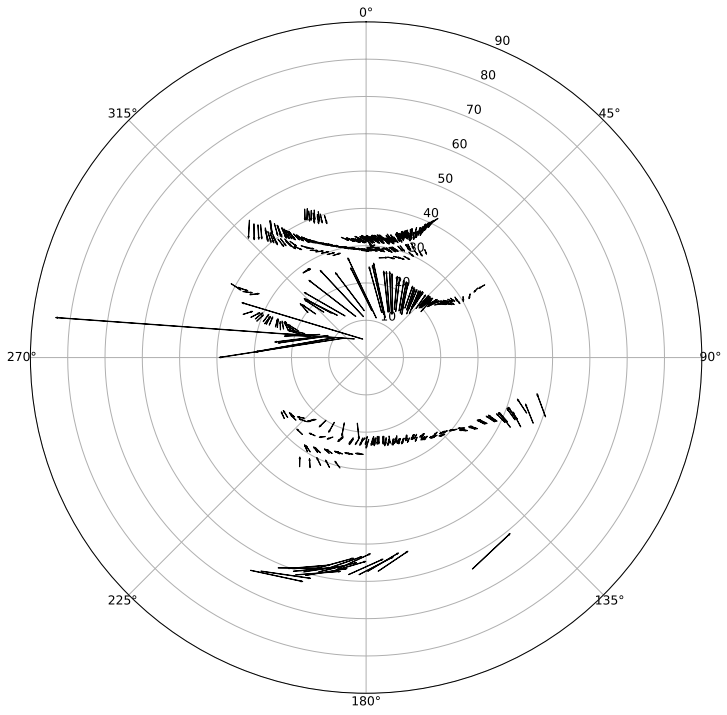

Figure 13: The residuals between the model and the data. All arrows are scaled by a factor of 60, which means 1° in the plot equals 1′ in reality.

function	squared residuals
$f(x)$	0.274
$g(x)$	0.233

Table 3: Squared residuals of the fit of $f(x)$ and $g(x)$ to the altitude residuals.

are two simple geometric functions that can describe this correlation:

$$f(x) = \frac{a}{\cos(alt + b)} + c$$
$$g(x) = \frac{a}{\tan(alt + b)} + c$$

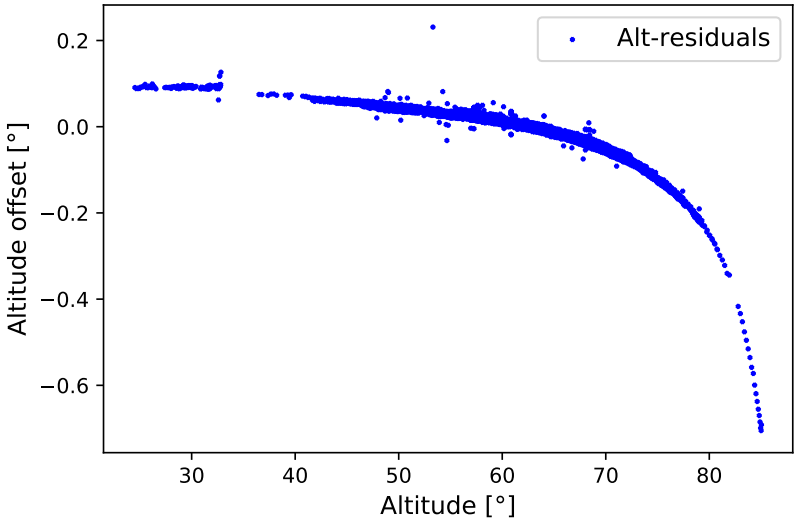

Figure 14: The residuals in altitude over the Altitude.

To find the function that describes this correlation better both function where fitted to the residuals in altitude and then the square residuals after the fit where calculated. The residuals after the fit are listed in Table 3. The residuals are slightly lower for the function $g(x)$. This can also be seen in Figure 15a and Figure 15b. The function $g(x)$ describes the data better at altitudes smaller than 30°. Because of that and because of the slightly lower residuals after the fit this function was used. However there is no physical reason to pick $g(x)$ over $f(x)$, they were both considered because they fit the data and are simple geometric functions. There is no known mechanical effect that would cause such a correction

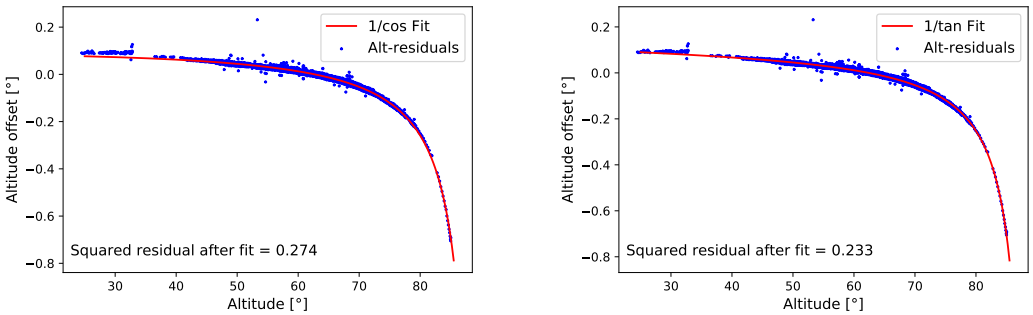

(a) Altitude residuals over the altitude with a $1/\cos$ fit.

(b) Altitude residuals over the altitude with a $1/\tan$ fit.

Figure 15: The altitude residuals over the altitude with different fit functions.

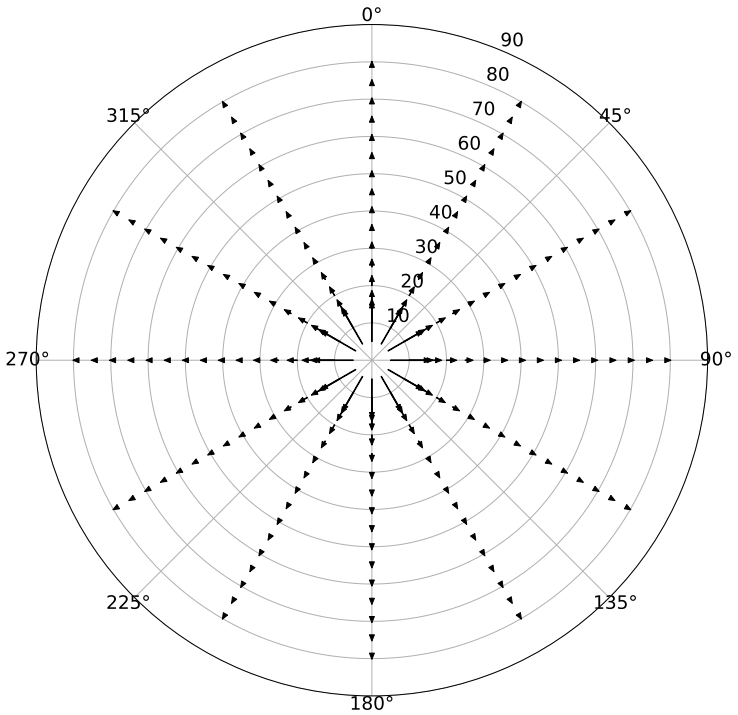

Figure 16: Demonstration of the effect of a the $a/\tan(alt + b)$ correction. The values for (a, b) are $(-1°, 90°)$.

factor. Furthermore, both functions diverge at $alt \to 90°$ to $-\infty$, which will cause

problems if the data contains large altitude values. In the mechanical model the $\frac{1}{\tan alt}$ correction was implemented by first calculating the angular offset in altitude this would cause

$$\delta alt = \frac{a}{\tan\left(alt + b\right)}, \tag{17}$$

and then rotating the vector by δalt degrees around the alt-axis as described in Equation 9 and Equation 10. The parameter c was not used since it just describes a constant shift in altitude, which is already taken into account by the parameter Δalt. The effect of this correction can be seen in Figure 16.

4.3.2 Azimuth Residuals

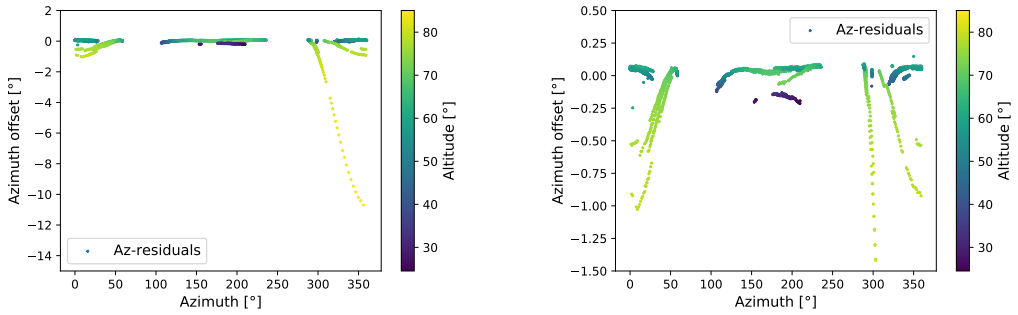

(a) (b)

Figure 17: The residuals in azimuth over the azimuth angle. The data points are coloured by their altitude.

The residuals in azimuth over the azimuth are plotted in Figure 17. At an azimuth angle of 300° the azimuth offset reaches as low as −12° as can be seen in Figure 17a. This occurs at an altitude angle of ∼ 85°. This large offset here can in part be explained by the fact that the azimuth angle becomes undefined as the altitude reaches ±90°, which is why in Figure 17b they are cut to see the dependence of the azimuth residuals on the azimuth for smaller altitudes. In the range from 320° to 50° there seems to be a cosine dependence of the azimuth residuals to the azimuth for altitude angles $> 60°$, but this effect is neither observed in the azimuth range of $[100°, 240°]$, nor in the azimuth $[310°, 50°]$ for altitude angles smaller than 55°. It is unclear whether this is because in those ranges there are a lot of data points, so the fitting algorithm favours minimising residuals and leaves larger residuals in areas with less data points, or if there is a complex dependence on both the azimuth and altitude angle. Pointing runs over the whole sky with

an isotropic distribution would make it possible to make this distinction, but unfortunately they were not available at the time of writing this thesis. Therefor no term correcting the azimuth offset was implemented into the fitting algorithm.

4.4 Application of the Improved Model

To see the impact of the altitude correction term introduced in subsubsection 4.3.1 the model is again fitted to the data as described in subsection 4.2. The fitted

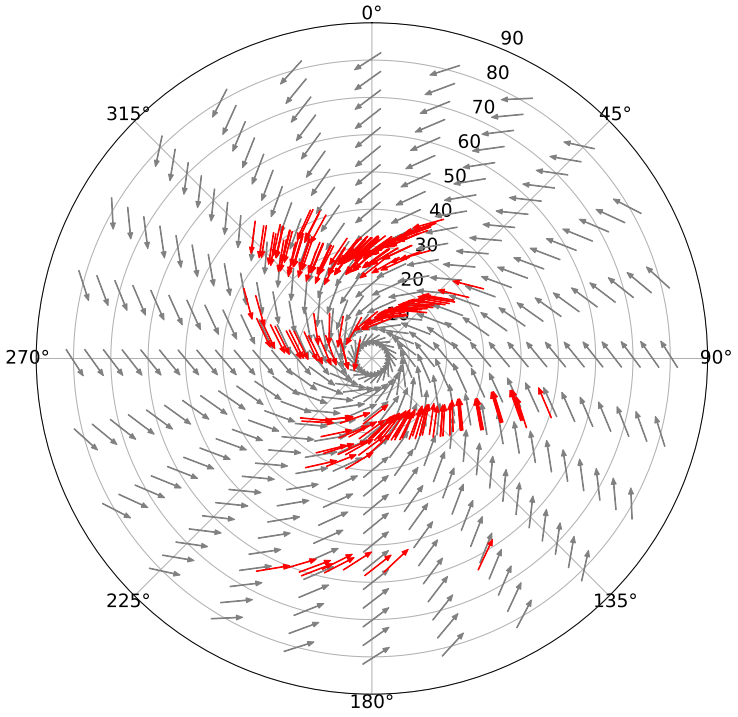

Figure 18: Black arrows is the difference between the optical axis of the MAGIC telescope and the reconstructed direction of the PointingCCD, grey arrows are the model fitted to the data with the $1/\tan$ correction. All arrows are scaled by a factor of 3.

model and the data points are plotted in Figure 12 and the fitting parameters compared to the parameters without the $1/\tan$ correction can be found in Table 4. The largest differences to the previous fit, caused by the introduction of the two new parameters, are for the parameters β and δ. The large difference for β can be explained by the fact that β is very small ($0.02°$) and therefor very sensitive to the

parameter	fitted-value	fitted-value without $1/\tan$	percentage-difference
Δalt	$-2.005°$	$-1.903°$	5.09 %
Δaz	$1.600°$	$1.538°$	3.88 %
λ	$243.982°$	$235.456°$	3.49 %
β	$0.020°$	$0.017°$	15 %
δ	$-0.602°$	$-0.663°$	10.13 %
a	$0.048°$		
b	$92.800°$		

Table 4: Parameter of the fit of the model to data from the MAGIC telescope and the PointingCCD with and without the $1/\tan$ correction.

introduction of new corrections. The correction caused by λ and β also increases with altitude (see Figure 9). Since the $1/\tan$ correction is strongly dependent on altitude (see Figure 16), corrections that have a dependence on altitude are more impacted than those who don't. This also explains why the difference for δ is 10 % while the corrections for Δalt and Δaz are around 5 %. To see how much the introduction of the $1/\tan$ correction has improved the model the residuals are again calculated and can be seen in Figure 19. In Figure 19a and Figure 19b one can see that the residuals in altitude have significantly decreased. In Figure 19b most of the residuals, except at high altitude angles of over 85° are nearly parallel to the zenith lines, which means only residuals in azimuth remain. This can also be seen in Figure 19c, although there still seems to be a small linear decline of altitude residuals with increasing altitude for altitude angles lower than 75° followed by an strong increase near the zenith. It is not clear though whether this strong increase is a real effect, since the $1/\tan$ correction does seem to fit the residuals quite well for large altitude (see Figure 15b). The strong increase could also be caused by the fact that there are only a hand full of data points above an altitude angle of 85°. Since the minimizer optimises for all data points areas with high density of data points are favoured and strong deviations on a few points don't have much weight. To test this isotropic pointing runs again would be needed. The azimuth residuals after the application of the $1/\tan$ correction are depicted in Figure 19d. As expected they still look very similar to the residuals before the correction (see Figure 17b). To get an idea of how accurate the model can be the residuals in altitude are plotted into a histogram and a Gaussian distribution of the form

$$h(x) = \frac{1}{\sqrt{2\pi\sigma^2}} \cdot \exp\left(\frac{(x-\mu)^2}{2\sigma^2}\right) \tag{18}$$

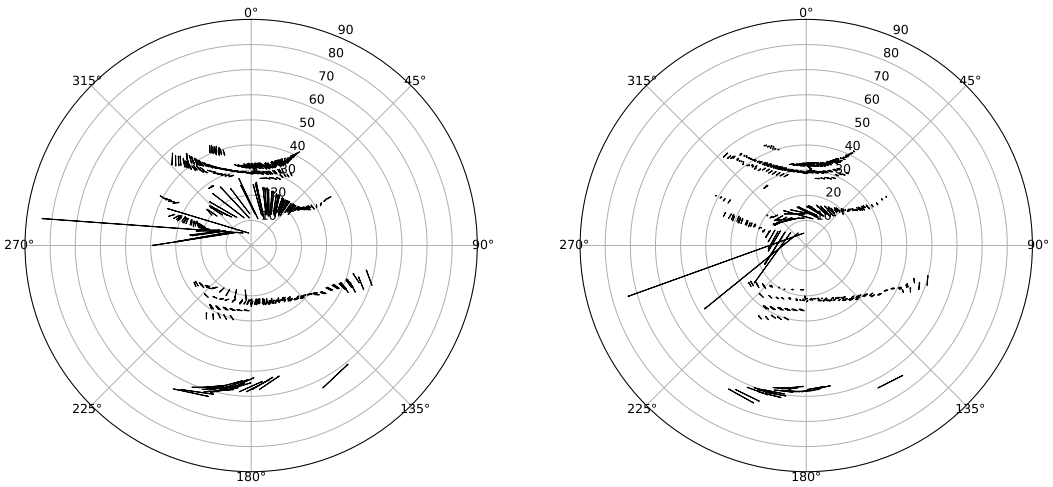

(a) Residuals in a polar plot before the 1/ tan correction. All arrows are scaled by a factor of 60 so that 1° equals 1′

(b) Residuals in a polar plot after the 1/ tan correction. All arrows are scaled by a factor of 60 so that 1° equals 1′

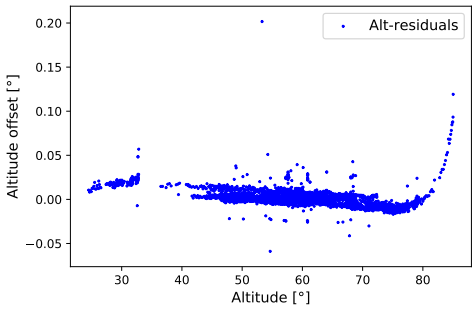

(c) Residuals in altitude over altitude

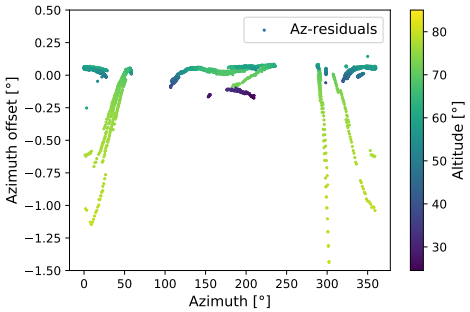

(d) Residuals in azimuth over azimuth. The data points are coloured with their altitude angle

Figure 19: (a) and (b): Comparison of the residuals before and after the 1/ tan correction in a polar plot.
(c) and (d): Altitude/azimuth residuals over altitude/azimuth after fitting the model with the 1/ tan correction to the data.

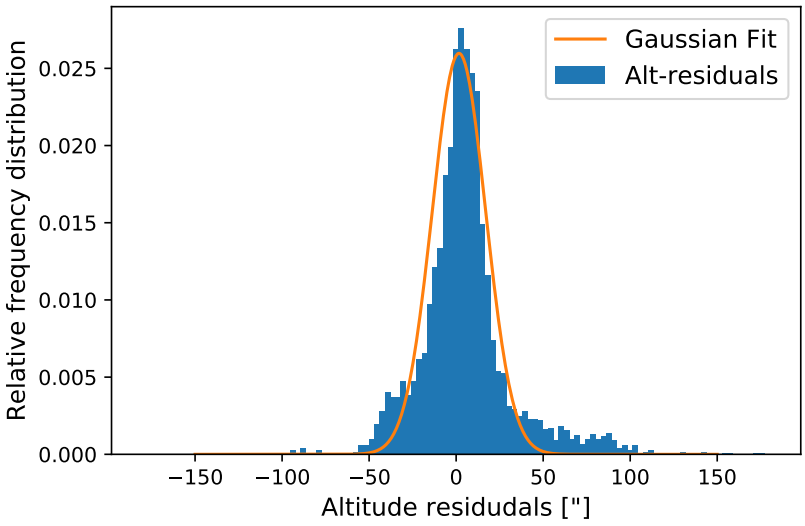

Figure 20: Normalised histogram plot of the altitude residuals with a Gaussian fit.

is fitted (see Figure 20). The fitted parameters are

$$\mu = 1.628'' \pm 0.186''$$
$$\sigma = 15.360'' \pm 0.124''.$$

The altitude residuals in Figure 20 still don't perfectly match a Gaussian distribution, residuals with altitudes around $-50''$ and $80''$ are more likely than if they were distributed Gaussian, which indicates there is another effect that has yet to be accounted for as described earlier in this chapter. Unfortunately because of time constraints this could not be investigated further. Despite that the relatively small standard deviation of $15.4''$ gives confidence in the approach of this mechanical model.

4.5 Altitude Hysteresis Effect

The software that is currently used to determine the pointing for the MAGIC telescope has an explicit term to correct for a hysteresis effect (Romaszkiewicz, 2006). This is achieved by adding or subtracting a constant factor depending on the direction the telescope is travelling in. To check whether this effect can also be observed in this model the altitude derivative at every point was taken by subtracting the two data points next to the current point in the MAGIC log files

$\dot{alt}$	m	t
> 0	$-1.42\,''\,^{\circ -1} \pm 3.12 \times 10^{-6}\,''\,^{\circ -1}$	$89.97'' \pm 1.07 \times 10^{-2}''$
< 0	$0.20\,''\,^{\circ -1} \pm 1.985 \times 10^{-6}\,''\,^{\circ -1}$	$-6.29'' \pm 6.55 \times 10^{-3}''$

Table 5: Fit-parameter for the linear fit to test for hysteresis.

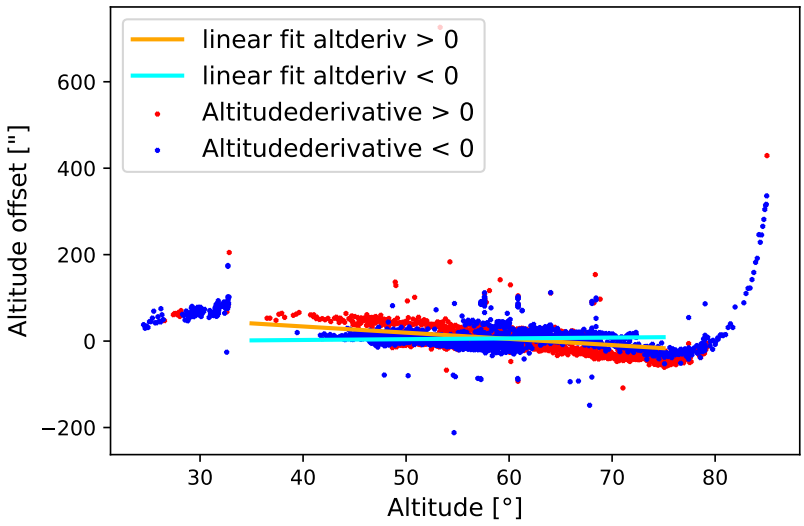

Figure 21: Altitude residuals over altitude coloured by the altitude time derivative. Red means altitude is increasing, blue means decreasing. The orange line is the linear fit for increasing altitude, the cyan line for decreasing. Both fits were done in the range 30° to 70°

and dividing by the time difference.

$$\dot{alt}_i = \frac{alt_{i+1} - alt_{i-1}}{t_{i+1} - t_{i-1}} \tag{19}$$

The residuals with the corresponding travelling direction is plotted in Figure 21. It looks like there is indeed a hysteresis effect that is depending on the altitude, so two linear fits were performed in the range $[30°, 70°]$, where the trend is linear. The resulting fit parameters are listed in Table 5.

Since the gradient of the straight line is quite different for the two fits, $-1.42\,''\,^{\circ -1}$ compared to $0.20\,''\,^{\circ -1}$, this hysteresis effect can't be explained with a constant shift depending on the travelling direction of the telescope, instead a linear shift with two parameters that depends on the altitude would be needed. Because of time constrains this was not implemented into the fitting algorithm.

5 Summary and Outlook

In this thesis, a mechanical model that describes the mis-pointing of a telescope has been developed. It consist of a three terms. The first one describes a constant offset between the telescope and the PointingCCD. The second one describes the effect of the non-verticality of the azimuth axis and the third describes the non-perpendicularity between the altitude and azimuth axis.
The model was tested on simulated data and on images captured by a PointingCCD installed on the MAGIC telescope. It was discovered that the model didn't describe the telescope completely. To correct for the residuals in altitude a fourth term proportional to one over the Tangent of the altitude was introduced. With this correction applied the residuals in altitude nearly followed a Gaussian distribution with a mean of $1.6''$ and a standard deviation of $15.4''$. A function describing the residuals in azimuth was not found.
An altitude hysteresis effect was discovered that was not explained by a constant offset depending on the altitude derivative but had a linear dependence on the altitude.
To improve the current mechanical model and to find an azimuth correlation pointing runs will be needed. The altitude hysteresis effect should be further investigated and included in the model. Furthermore the model can be expanded to include data using the LEDs and stars projected on the lid of the Cherenkov camera to describe the mechanical deformations of the telescope.
Lastly the completed mechanical model needs to be tested on a MST of the CTA to see how well it is suited to describe the pointing of the CTA.

Literaturverzeichnis

References

H. J. Völk; K. Bernlöhr. Imaging very high energy gamma-ray telescopes. *Experimental Astronomy*, 25:173, 2009. URL `https://arxiv.org/pdf/astro-ph/0512184.pdf`.

Ciro Bigongiari. The magic telescope. *proceedings of HEP2005 International Europhysics Conference on High Energy Physics EPS*, 2005. URL `https://arxiv.org/pdf/astro-ph/0512184.pdf`.

CTA collaboration, 2019. URL `https://www.cta-observatory.org/`. [Online; accessed 23-June-2019].

The EHT Collaboration et al. First m87 event horizon telescope results. i. the shadow of the supermassive black hole. *ApJL*, 875:1, 2019. URL `https://iopscience.iop.org/article/10.3847/2041-8213/ab0ec7`.

Jakob Herbich. Testing a Single-CCD-Concept for the H.E.S.S. II Pointing, 2010. Bachelor Thesis.

Steven G. Johnson. The nlopt nonlinear-optimization package, 2019. URL `http://github.com/stevengj/nlopt`.

P. Kaelo and M. M. Ali. Some variants of the controlled random search algorithm for global optimization. *Journal of Optimization Theory and Applications*, 130 (2):253–264, 2006.

Dirk Lennarz. *A Study of Transient Very-High-Energy Gamma-Ray Emission from Gamma-Ray Bursts and Supernovea with H.E.S.S.* PhD thesis, Ruprecht-Karls-Universität Heidelberg, 2012.

Robert Wagner. The magic telescope at night. `https://en.wikipedia.org/wiki/MAGIC_(telescope)`, 2004. [Online; accessed 23-June-2019].

Anna Julia Romaszkiewicz. *Investigation of the position accuracy of the MAGIC of telescope with the help of Starguider CCD camera*. PhD thesis, Max-Planck-Institut für Physik Werner-Heisenberg-Institut, 2006.

Deirdre Horan Scott Wakely. Tevcat, 2016. URL `http://tevcat2.uchicago.edu/`. [Online; accessed 23-June-2019].

Domenico Tiziani. Investigations towards a Single-CCD Pointing-Solution for the Medium-Sized Telescopes of the Cherenkov Telescope Array. Master's thesis, Friedrich-Alexander-Universität Erlangen-Nürnberg, 2015.

Wikipedia contributors. Messier 87 — Wikipedia, the free encyclopedia. `https://en.wikipedia.org/w/index.php?title=Messier_87&oldid=900005454`, 2019. [Online; accessed 24-June-2019].

Danksagung

An dieser Stelle möchte ich mich bei Allen bedanken, die mich bei der Erstellung dieser Arbeit unterstützt haben. Vielen Dank an

- Prof. Dr. Christopher van Eldik für die Vergabe des Themas, die wöchentlichen Diskussionen und die stets gute Betreuung meiner Bachelorarbeit
- Prof. Dr. Gisela Anton für die Übernahme der Zweitkorrektur
- Domenico Tiziani für die vielen Gespräche und gute Betreuung
- Allen Mitgliedern der Pointing-Gruppe des ECAPs
- Felix Beier und Domenico Tiziani für das Korrekturlesen meiner Arbeit
- Allen Mitgliedern des Büros 108a für die stets angenehme Stimmung und Versorgung mit Süßigkeiten
- Meinen Eltern für die Unterstützung während meines gesamten Studiums.

Erklärung

Hiermit bestätige ich, dass ich diese Arbeit selbstständig und nur unter Verwendung der angegebenen Hilfsmittel angefertigt habe.

Erlangen, den 25. Juni 2019

Olaf Tönsing